Chemistry–A European Journal
Research Article
doi.org/10.1002/chem.202401796
Chemistry Europe
European Chemical Societies Publishing
www.chemeurj.org

Unravelling the Mechanism of CO_2 Activation: Insights Into Metal-Metal Cooperativity and Spin-Orbit Coupling with {3d–4f} Catalysts

Purva Dua,[a] Asmita Sen,[a] and Gopalan Rajaraman*[a]

Converting CO_2 into useful chemicals using metal catalysts is a significant challenge in chemistry. Among the various catalysts reported, transition metal lanthanide hybrid {3d–4f} complexes stand out for their superior efficiency and site selectivity. However, unlike transition metal catalysts, understanding the origin of this efficiency in lanthanides poses a challenge due to their orbital degeneracy, rendering the application of DFT methods ineffective. In this study, we employed a combination of density functional theory (DFT) and ab initio CASSCF/RASSI-SO calculations to explore the mechanism of CO_2 conversion to cyclic carbonate using a 3d–4f heterometallic catalyst for the first time. This work unveils the importance of 3d and 4f metal cooperativity and the role of individual spin-orbit states in dictating the overall efficiency of the catalyst.

Introduction

Carbon dioxide (CO_2) is one of the significant components of greenhouse gases in the atmosphere, responsible for global warming.[1,2] In the last few years, the concentration of this greenhouse gas in the troposphere has been increasing at an alarming rate, and the only way to utilise this abundant, non-toxic chemical waste is to use it in the carbon capture technologies generating various value-added feedstocks.[3,4,5] Among several avenues that are available,[6,7,8] one of the most promising pathways is the catalytic conversion of CO_2 to cyclic carbonates utilising epoxide.[9,10] Cyclic carbonates are formed with 100% atom efficiency and can be extensively used as green polar aprotic solvents, lithium-ion batteries, fuel additives, and chemical intermediates. However, owing to the very high thermodynamic stability and kinetic inertness, the conversion of CO_2 to value-added chemicals is found to be difficult without metal catalysts. While there are several catalysts proposed for this important catalytic conversion, utilisation of only transition metal/Lewis acids as catalysts was found to be sluggish, and incorporation of Ln(III) ion in the catalytic design was found to yield a large turnover number(TON)/ turnover frequency(TOFs) (Figure S1). Particularly, {3d–4f} clusters are found to be attractive targets for this conversion, and this is evident from numerous such catalysts reported,[11,12,13] though the reason for such a combination is elusive.

Among several {3d–4f} catalysts reported, $[LnZn_3L_4]$[14] complexes (H_2L=N-(2-((2-hydroxy benzylidene) amino) ethyl)-2-hydroxy benzamide and Ln=Gd(III) (**1**), Dy(III) (**2**), Er(III) (**3**)) proven to be highly effective in the formation of cyclic carbonates with the TOF as high as 38.000 h^{-1} are reported with a very low-catalyst loading (0.001 mol%) and solvent-free conditions under the temperature of 120 °C and 10 bar pressure in an autoclave setup (Figure 1). A careful analysis of this set of lanthanide complexes reveals that the nature of the Ln(III) ion also plays a crucial role in dictating the TOF value, with Er(III), in particular, found to yield superior values. A thorough literature survey reveals that this is true also for other {3d–4f} catalysts where Er(III), in general, promote robust CO_2 conversion compared to other lanthanides.[15,16] While there are several mechanistic studies that explore the activation of CO_2 to cyclic carbonates using transition metal catalyst,[17,18,19,20] exploring such mechanism for {3d–4f} catalyst is challenging due to (i) paramagnetic Ln(III) ions have orbitally degenerate ground state and large spin-orbit coupling (except Gd(III)). Therefore, an approach beyond DFT methods is required to address the problem (ii) computing the potential energy surface of such catalytic transformations in multimetallic clusters poses various mechanistic challenges as there are several sites available for the reactivity. In the present work, employing DFT and *ab initio* CASSCF/RASSI-SO method, we have explored the mechanism of CO_2 activation using complexes **1**–**3** to answer the following open question in this area. i) do the 4f metal ions play a role in catalytic conversion? (ii) does the efficiency of the reaction alter due to the nature of the Ln(III) ion and its corresponding spin-orbit states?

As catalyst **1**–**3** was reported to yield very high TOF for this reaction, with the trend mimicking the other {3d–4f} catalyst, we have explored these complexes to answer several open questions in this area. Our initial focus is on complex **1** as Gd(III) can be treated with DFT methods, which yield S = 7/2 as ground state as expected, with the other spin-states lying more than 200 kJ/mol higher in energy and are not relevant for the mechanistic studies (see Table S1). Later on, the CASSCF/RASSI-SO method was employed on computed species considering

[a] P. Dua, A. Sen, Prof. G. Rajaraman
Department of Chemistry, Indian Institute of Technology Bombay, Powai, Mumbai-400076, India
Tel: (+91)-22-2576-7183
E-mail: rajaraman@chem.iitb.ac.in

Supporting information for this article is available on the WWW under https://doi.org/10.1002/chem.202401796

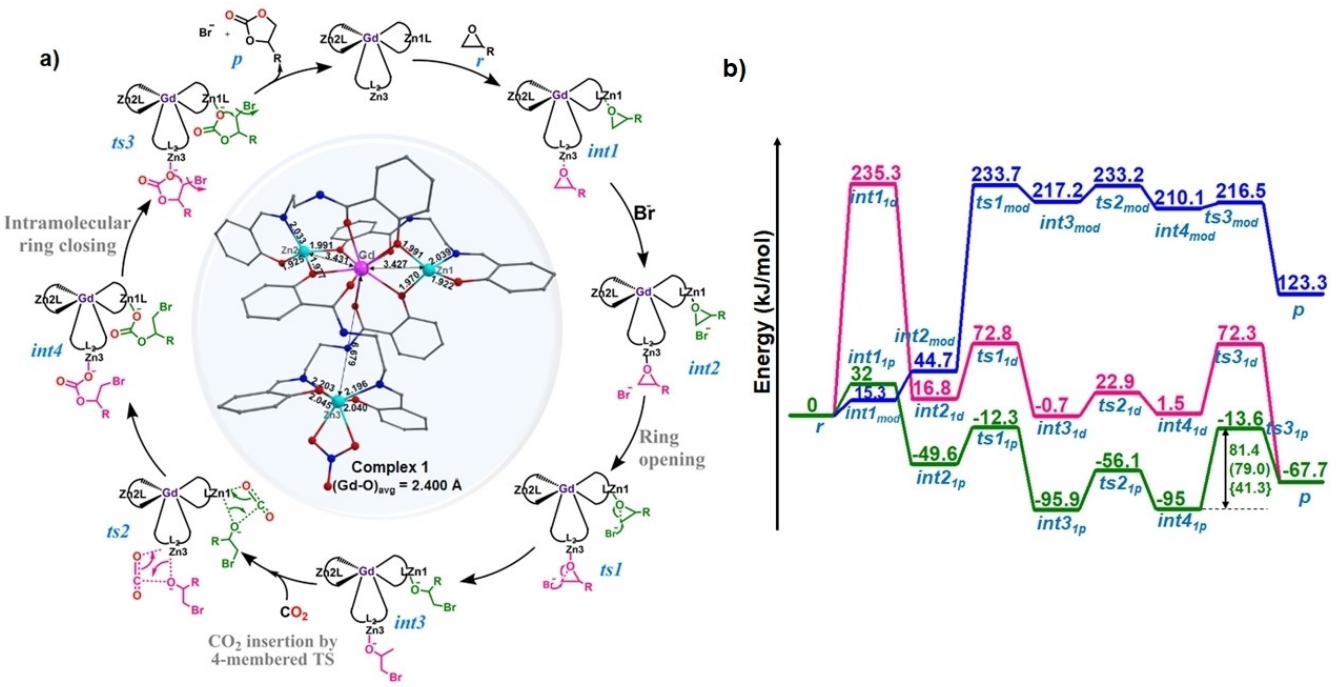

Figure 1. (a) Schematic representation of cycloaddition reaction between epoxide and CO_2 forming cyclic carbonate employing {3d–4f} catalyst (**1**) and (b) corresponding potential energy surface (PES; ΔG) at proximal (green) or distal site (pink). Blue lines show the PES for the modelled proximal Zn. The energies of the rate-determining steps (rds) for complex **2** and **3** are shown in () and {} respectively.

Dy(III) and Er(III) to answer the role of various spin-orbit states in influencing reactivity.

Results and Discussions

Complex **1** is a tetrametallic cluster with the octacoordinated Gd(III) ion with an average Gd–O bond length of 2.4 Å (Figure 1). The Gd(III) ion is situated inside the cavity surrounded by two Zn(II) ions (Gd···Zn1 and Gd···Zn2 distances of 3.431 Å and 3.427 Å, respectively; termed as proximal Zn sites) connected by two μ_2-alkoxo bridges. Further, there is also an additional Zn(II) ion (Gd···Zn3 distance of 6.679 Å; termed as distal Zn site). The proximal Zn(s) have a tetrahedral environment coordinated to three oxygen centres and one nitrogen centre of the salen ligand. However, the distal Zn metal is hexacoordinated and ligated with two nitrogen centres, two oxygen centres of salen ligand and a nitrate ion. The mechanism adapted considers both distal and proximal Zn ions, as shown in Figure 1a. The optimised structure of all the species involved in the catalytic pathway for proximal and distal sites are shown in Figures 2 and 3, respectively. To begin with, the epoxide coordinates with the Zn sites, leading to the formation of an intermediate (***int1***) is assumed. The formation of this species is found to be endothermic for both distal and proximal sites by 235.3 kJ/mol and 32.0 kJ/mol, respectively. Despite the geometric equivalence of the two proximal sites, which implies similar energetics, we conducted additional calculations on ***int1***, where CO_2 binds to the second proximal site of the Zn2 center. The resulting formation energy was found to be endothermic and differed by only ~2 kJ/mol for the Zn1 site, confirming our initial observations regarding the equivalence of Zn1 and Zn2. Here after we have restricted our studies to Zn1 center only.

For the distal site, endothermicity is prohibitively high, suggesting that the reaction is unlikely to proceed via this intermediate/pathway. Unlike the proximal Zn site, which has tetrahedral geometry, the distal Zn is six-coordinated and requires cleavage of the nitro-groups prior to the epoxide coordination, escalating the energy penalty by several hundred kJ/mol. Further, the Lewis acidity of the proximal Zn ions is found to be higher compared to the distal Zn, reflected in the computed NPA charges (Table S2 and Table S3). In the next step, Br^- from TBAB is assumed to enter the coordination sphere stabilised by the non-covalent interactions (***int2***) and formation of which is stabilised compared to ***int1*** by 218.5 kJ/mol and 81.6 kJ/mol for the distal and proximal sites (Figure S2), respectively. While the reaction is exothermic with respect to the reactant for the proximal site, for the distal site, it is slightly endothermic. At ***int2***$_{1p}$, the Zn–O(epoxide) bond is significantly strengthened due to charge transfer from the Br^- (2.301 vs 2.173 Å), and this also adds to the stability of this species. The stronger Zn–O bond weakens the epoxide O–C bond, facilitating a ring-opening attack by the Br^- ion via ***ts1***$_{1p}$ (***ts1***$_{1d}$) in the next step with an estimated barrier of 37.3 (56.0) kJ/mol from the preceding species. For the proximal site, from the reactant, there are no barriers, suggesting a facile reaction. In the subsequent stage, we postulate the formation of ***int3*** which is exothermic for both the proximal (Figure 2d) and distal (Figure 3d) sites (73.5 kJ/mol and 83.6 kJ/mol, respectively). Rela-

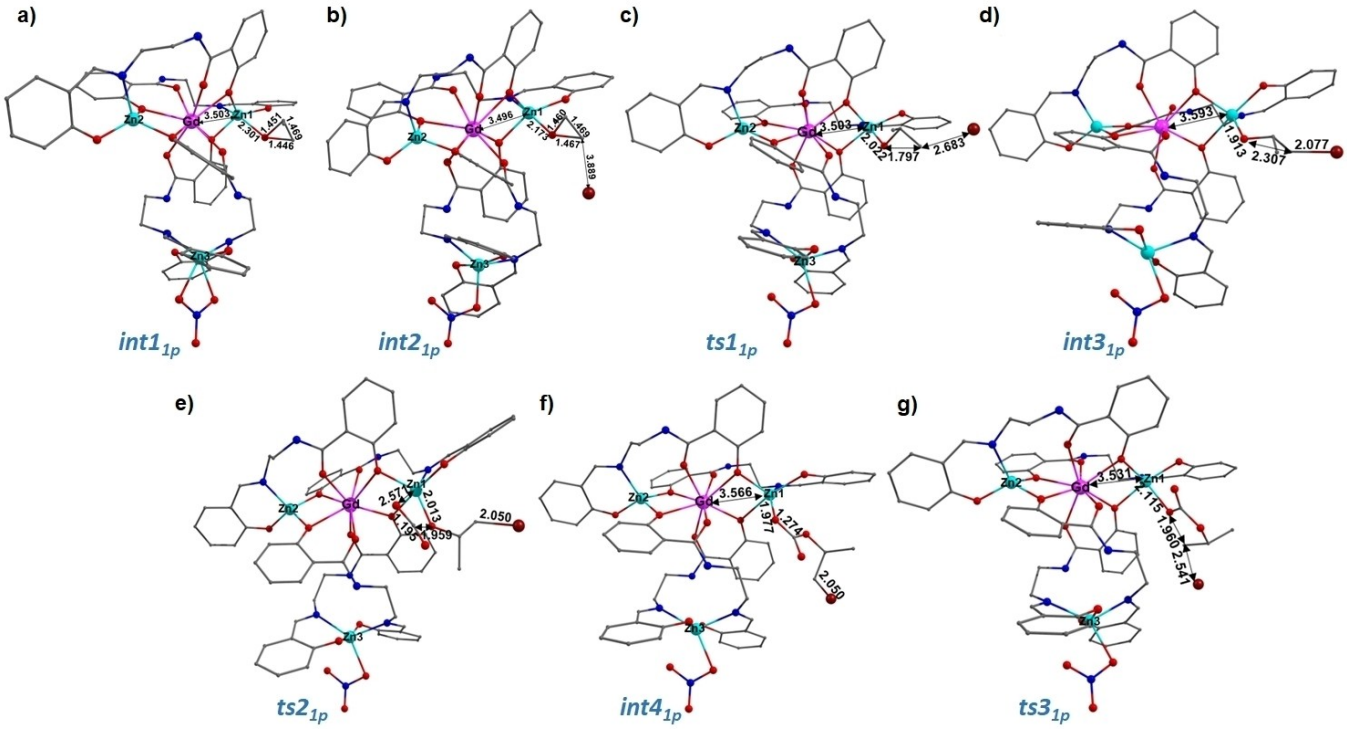

Figure 2. DFT optimised geometries of (a) ***int1***$_{1p}$, (b) ***int2***$_{1p}$, (c) ***ts1***$_{1p}$, (d) ***int3***$_{1p}$, (e) ***ts2***$_{1p}$, (f) ***int4***$_{1p}$, (g) ***ts3***$_{1p}$ of the Proximal Zn site showing important bonding parameters. Gd – pink, Zn – cyan, O – red, N – blue, C –grey, Br – maroon. Hydrogens are omitted for clarity.

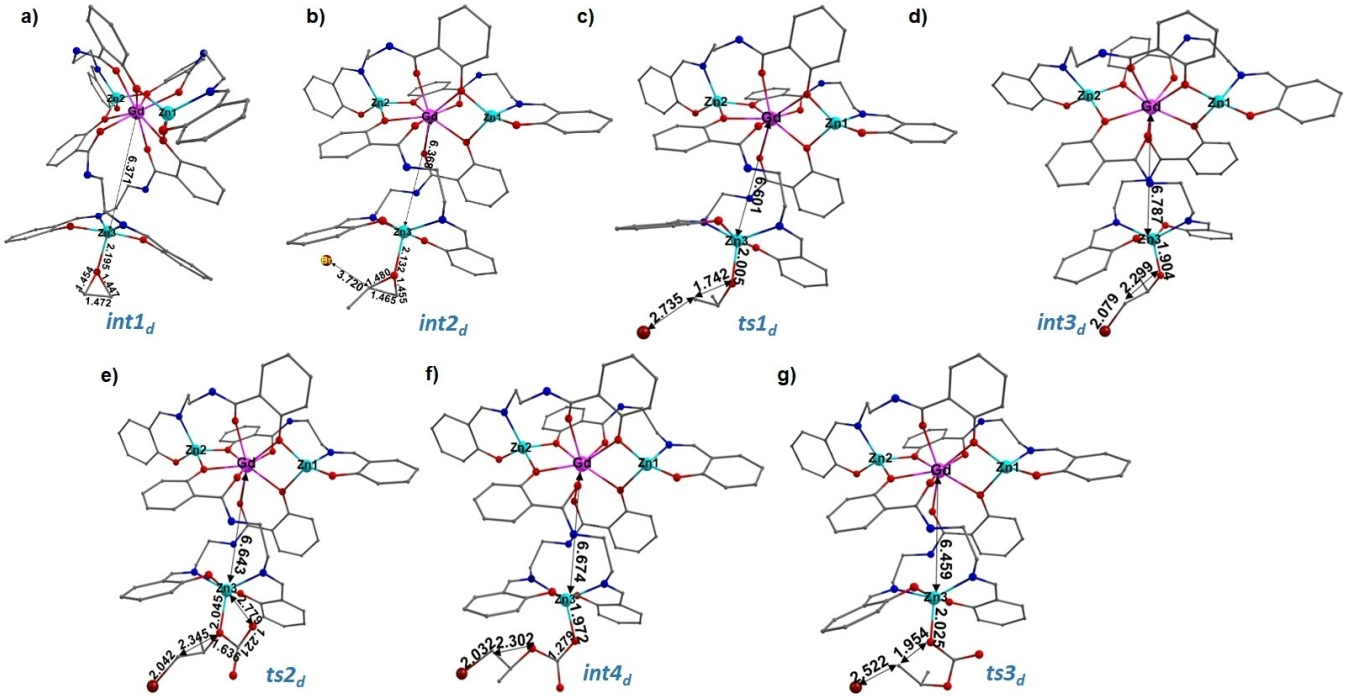

Figure 3. DFT optimised geometries of (a) ***int1***$_{1d}$, (b) ***int2***$_{1d}$, (c) ***ts1***$_{1d}$, (d) ***int3***$_{1d}$, (e) ***ts2***$_{1d}$, (f) ***int4***$_{1d}$, (g) ***ts3***$_{1d}$ of the distal Zn site showing important bonding parameters. Gd – pink, Zn – cyan, O – red, N – blue, C –grey, Br – maroon. Hydrogens are omitted for clarity.

tively larger exothermicity for the proximal site is due to the presence of Gd(III) ion in its second coordination sphere.

In the next step, CO_2 is expected to be inserted where the O···CO_2 bond is expected to form via ***ts2***$_{1p}$ with a barrier of 39.8 kJ/mol from ***int3*** but a barrier-less process from the

reactant perspective. At the distal site, the barrier is calculated to be 23.6 kJ/mol from the ***int3*** species. Notably, this barrier value is comparable when estimated from the reactant species. While the Zn···O distance in the proximal site (Figure 2e) is 2.571 Å, the same is found to be higher in the distal site (Figure 3e) (2.779 Å), indicating a weaker Zn···O interaction in the latter one, resulting in a more flexible four member transition state and attributing to a lower energy barrier.

In the next step, the O···C bond formation completes and leads to the formation of ***int4***, which is nearly thermoneutral for both pathways, as compared to ***int3***. In the next step, the formation of cyclic carbonate is expected via ***ts3***$_{1p}$ (***ts3***$_{1d}$) with a barrier of 81.4 (70.8) kJ/mol, followed by the product formation and regeneration of the catalyst. This step is found to have the steepest energy barrier among all, suggesting that this is the rate-limiting step for the reaction. For the proximal site, this is still favourable due to the overall gain in thermodynamics, while in the distal site, the barriers are significant, again ruling out the reactivity via the distal Zn sites.

The experimental turnover TOF for the reaction of **1** is reported to be 4600 h^{-1} in 10 mmol of epoxide and 120 °C temperature. Using energetic span approximation[21] (shown in Equation S1 in supporting information), the calculated TOF for this reaction is determined to be 3447 h^{-1}. This is in agreement with the experimental value, though it is slightly underestimated and this is correlated to various experimental factors (autoclave reaction) that are not fully captured in the energetic-span model.

Further, we have performed single-point calculations for the rate-determining intermediate and transition states for catalysts **2** and **3**, and the barriers were estimated to be 79.0 and 41.3 kJ/mol, resulting in a reactivity trend of **3** > **2** > **1** (see Figure 1b). This finding is also supported by the experiments where there is a substantial difference in the TOF when the Ln(III) ions are Gd(III) vs. Dy(III) vs. Er(III). The overall potential energy surface for complexes **2** and **3** are shown in Figures S3 and S4, respectively. For complexes **2** and **3**, the formation of ***int1***$_{2p/3p}$ is found to be endothermic by 31.3 kJ/mol and 0.3 kJ/mol, respectively. While Dy(III) energy is similar to that of Gd(III), a substantial reduction has been witnessed for the Er(III) ion. A consistent pattern is also observed across other species, showing notable exothermicity for all species with Er(III) compared to the Dy(III) ion. These observations collectively suggest that catalyst **3**, associated with Erbium, is the most efficient catalyst among the studied ones.

To understand the intriguing effect of 4f-metal during the transition metal catalysis, we have estimated the second-order perturbation interactions in **1**, where we observed a prominent donor-acceptor interaction between the proximal Zn and Gd centre [Zn1(4s)→Gd(5d): 54.7 kJ/mol], while the distal Zn is found to be unaffected.[22] As the reaction proceeds in the proximal site, this interaction varies drastically in intermediates and transition states (Figure 4). For instance, a steep hike in the donor-acceptor interaction strength is observed in ***int1***$_{1p}$ (23.4 kJ/mol) followed by ***int2***$_{1p}$ (21.0 kJ/mol), indicating an enhanced electron delocalisation from Zn to Gd, which stabilises the stationary states and therefore, facilitates the

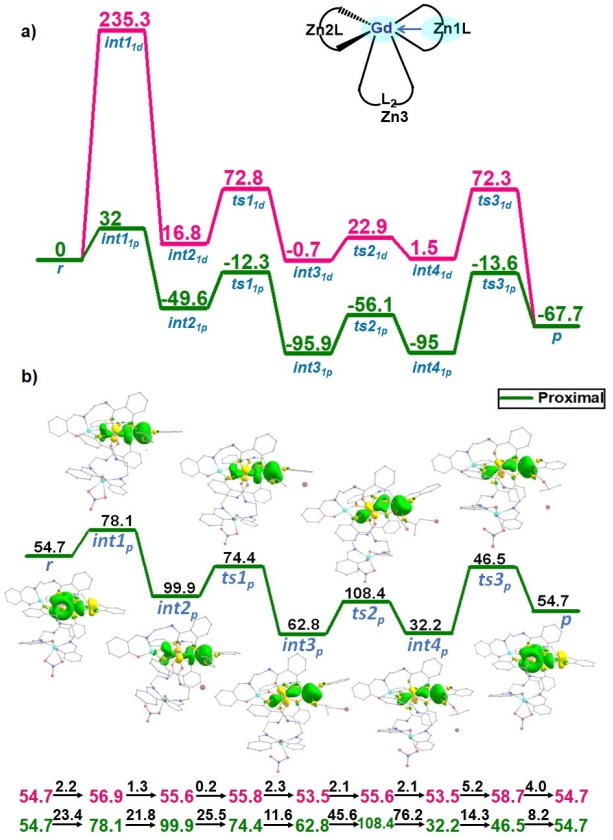

Figure 4. a) Computed PES (ΔG) for the mechanism in Figure 1b for the Distal(pink) and proximal(green) sites. b) NBO donor-acceptor interactions corresponding to Zn1(4s)→Gd(5d) orbitals (kJ/mol) for the proximal site pathway. The bottom values indicate the evolution of NBO second-order PT theory computed donor-acceptor interactions from Zn(II) to Gd(III) centers, with pink and green representing distal and proximal sites, respectively. The value given in black above the arrow is the difference between two consecutive interactions.

reaction. Figure 4b represents the corresponding orbitals at proximal site and how it changes during the course of the reaction. In contrast, no donor-acceptor interaction was found between the Gd and distal Zn centre, however, we can expect a long-range influence due to the Zn1(4s)→Gd(5d) interactions in the proximal site while the reaction occurs in the distal position. This type of charge-transfer in 3d–4f complexes has been noted earlier.[23,24] During the reaction in the distal Zn centre, the change in Zn1(4s)→Gd(5d) interactions does not vary much as the reaction proceeds at the distal site and fluctuates within the range of 2–5 kJ/mol from the reactant species (see Figure S5 for the corresponding orbitals at distal site). This above fact clearly demonstrates the cooperative influence of 4d metal centres on the reactivity of 3d metal. A comparable trend is also evident for the Dy(III) compound, albeit with some of the donor-acceptor interactions appearing smaller for Er(III), aligning with the distinct characteristics of the lanthanide ions (refer to Figure S6 and S7).

To assess and analyse the role of 4f-ion cooperativity in the overall CO_2 conversion, we have carved out a mononuclear Zn(II) model from the proximal site and performed the overall

mechanism (see Figure S8). For this model, a drastic change in the reaction energetics is observed, with ***ts1***$_{mod}$ (Figure S9) found to have a barrier of 233.7 kJ/mol with a significant energy penalty for all steps, suggesting a significant catalytic hindrance once the Ln(III) ion is removed. This is supported by the experiments where binaphthyldiamino salen-type complex with similar ligand topology was found to yield only a fraction of TOF with harsher reaction conditions (450 h^{-1}).[25] The energy decomposition analysis reveals a major portion of the barrier in the model arises from positive interaction energy, while favourable negative orbital interaction energy was witnessed in the case of proximal sites (E_{int}: 68.3 kJ/mol vs. −151.2 kJ/mol). This directly indicates that the Gd(III) metal centre helps in reducing the intrinsic energy barrier for the reaction, indicating the existence of electronic cooperativity between the Gd(III) ion and the Zn(II) ion.

Apart from the given mechanistic consideration from DFT calculations, it is apparent that the nature of the Ln(III) ions also influences the catalytic reactivity. As Dy(III) and Er(III) ions are strongly anisotropic, a single reference method[26] such as DFT cannot be employed. To circumvent this problem, we have employed the geometry from the DFT calculations and performed CASSCF/RASSI-SO calculations on all the species in the potential energy surface to elucidate the role of spin-orbit coupled states and how the geometry around the Ln(III) alters the related SO states and influence the overall reaction. The eight Kramers doublets of Er(III) and Dy(III) are found to lie within a 4 kJ/mol energy margin for the proximal site, while in the case of the distal site, it is found to be relatively smaller, suggesting larger influence of SO states at the proximal sites (Figure S10 and S11). Particularly as the reaction proceeds, the ground state m_J levels were found to alter significantly at the proximal site but only to a smaller extent at the distal site. This is essentially due to the fact that alteration in the proximal site, alters the overall charges in the bridging atoms that are common to Zn and Ln(III) ions, and this alteration in the charge varies the stability of the corresponding m_J states. In the realm of Ln(III) single-molecule magnets, this has been well studied and explained, where relative charges on the axial and equatorial positions dictate the corresponding ground state.[27] The variation of $m_J = 13/2$ at the ground state to $m_J = 11/2$ at the transition state suggests variation in the electronic configurations that offer additional flexibility both for the Er(III) complex (Figure 5) as well as for the Dy(III) (Figure S12) ions. These additional low-lying spin-orbit states can lower the kinetic barrier, facilitating faster reactions. To ascertain this point, the lower barrier observed for Er(III) and Dy(III) was due to variation in the electronic configurations during the course of the reactions as revealed by the CASSCF/RASSI-SO calculations, we have computed the corresponding β-electron densities from both CASSCF/RASSI-SO as well as from DFT calculations on the Er(III) and Dy(III) ions at the rate-limiting step (***ts3***). As the electron density in both calculations is similar, this offers a chance to understand the role of prolate vs oblate ions in the catalytic cycle. Particularly, while Dy(III) at the proximal site was found to be similar at rate-determining step (Figure S13), the nature of the electron density varied significantly for the Er(III) (see Figure 5 inset), suggesting that its SO states are more amenable during the course of the reaction offering further flexibility for the conversion of CO_2 to cyclic carbonates – an observation which is hitherto unprecedented.

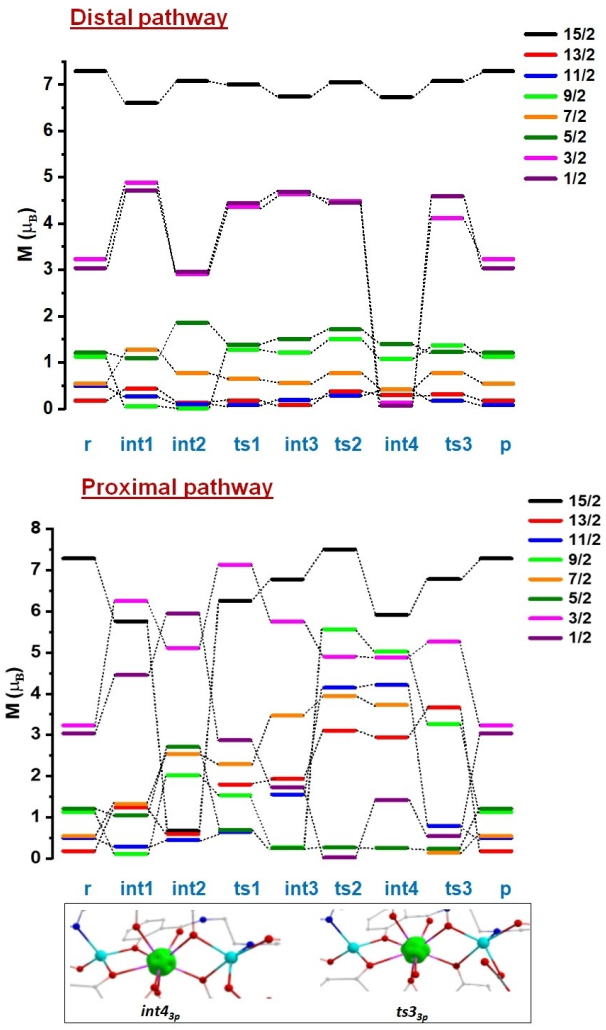

Figure 5. CASSCF/RASSI-SO/SINGLE_ANISO computed magnetic moments of each m_J state for complex **3** along the potential energy surface for distal(top) and proximal(bottom) pathways. The inset shows the electron density corresponding to the 4f orbitals of ***int4***$_{3p}$ and ***ts3***$_{3p}$ of **3**, showcasing alterations in their prolate shape along the reaction coordinate.

Upon analyzing the energy barrier for the rate -limiting step, it's evident that without Gd(III), the Zn(II) center exhibits a barrier height of 137.0 kJ/mol higher compared to when Gd(III) is present. This indicates that the participation of Gd(III) (and other Zn(II) ions) actively reduces the kinetic barrier, suggesting cooperative effects. Additionally, considering the absence of spin-orbit coupling in Gd(III), the disparity in barrier heights between Gd(III) and Dy(III) or Er(III) provides insight into the role of SOC. Specifically, the estimated differences are 2.4 and 40.1 kJ/mol for Dy(III) and Er(III), respectively. While this highlights a larger SOC role in Er(III) compared to Dy(III), the overall reduction in barrier heights underscores the dominance of cooperativity in kinetics. It is worth noting that SOC effects were assessed solely at the structural level with single-point

calculations, excluding geometric changes. Therefore, this study serves as a preliminary blueprint on the role of SOC in 3d-4f catalysis, suggesting that further detailed studies are essential to fully comprehend their roles.Conclusions

To this end, for the first time, a combination of DFT and CASSCF/RASSI-SO methods were used to study the conversion of CO_2 to cyclic carbonates. Our calculations reveal that the proximal Zn site, instead of being more sterically hindered is the more reactive site. This puzzling observation unearths the importance of 3d–4f metal cooperativity, which is found to lower the kinetic barrier for the rate-limiting ring-closure transition, resulting in the formation of cyclic carbonates. Given the strong anisotropy of Dy(III) and Er(III) ions, a single reference method like DFT may not suffice, leading us to employ a combined approach involving geometry from DFT calculations and subsequent CASSCF/RASSI-SO calculations to explore the role of spin-orbit coupling in reactivity. Our discoveries reveal the intricate role of spin-orbit coupled states, where we observed alterations in the corresponding ground m_J state as we progress along the reaction coordinate. They underscore the added flexibility provided by low-lying spin-orbit states, which is particularly noticeable in Er(III) complexes. These insights not only elucidate the underlying mechanisms but also offer prospects for optimising the catalytic pathways, as demonstrated by the lower kinetic barriers observed for Er(III) and Dy(III) ions in the conversion of CO_2 to cyclic carbonates. Analyzing the energy barrier for the rate-limiting step reveals that the absence of Gd(III) significantly heightens the Zn(II) center's barrier, indicating active reduction by Gd(III) and suggesting cooperative effects; furthermore, comparing barrier heights with Dy(III) and Er(III) elucidates the role of spin-orbit coupling, emphasizing cooperativity's dominance in kinetics.

Computational Details

We have performed the DFT calculations for Gd (III) using the Gaussian 09 suite of programs[28] and post-Hartree–Fock ab initio calculations for asymmetrically filled Dy (III) and Er (III) using the MOLCAS 8.0 code.[29] The geometries were optimised using B3LYP-D3 functional,[30] which incorporates the dispersion proposed by Grimme. Three different basis sets were used; double-zeta (DZ) quality basis set employing Cundari–Stevens (CS) relativistic effective core potential (ECP) on Gd atom'[31,32]; SDD[33] for Zn and Br and 6-31G* basis set for the other atoms. The harmonic vibrational frequency calculations have been performed at 298.15 K to characterise the nature of all stationary points. All global minima are identified by all positive frequencies, while the transition state is indicated by a single imaginary negative frequency. The energies were refined by the single-point calculations on the DFT-optimized structures in the same level of theory. CRENBL basis set for Gd atom[34] and TZVP basis set for all other atoms. Therefore, the final energies are the single point gas phase energy and Gibbs free energy corrected higher-level electronic energies. For Dy and Er, the Gd geometries were assumed as the lanthanides are known to yield analogues structures.[35,36,37] However, we have compared the bond lengths of the first coordination sphere of the X-ray structures of all three complexes where the average deviation of Ln–O bond length is less than 0.01 Å, clearly suggesting that they these are structurally analogues as reported elsewhere (as shown in Figure S14). Single-point calculations are done for the Dy and Er complexes to compare the energies and reactivity of Dy, Gd and Er complexes. To validate the energies obtained through single reference DFT calculations for Dy and Er complexes, the beta electron densities are plotted and compared with the beta electron density obtained through SA-CASSCF calculations. Figure S9 represent the beta electron densities for the rate determining transition state and intermediate for **2** and **3** and they are similar to the one obtained from DFT suggesting that 4f electronic configuration predicted by SA-CASSCFand the DFT are the same. EDA analysis were performed using AOMix 6.6 version software[38] to understand the molecular contributions to reaction barriers using the distortion-interaction, or activation strain, method. All the calculations are carried out with the same B3LYP level of theory using an all-electron SARC-DKH2 basis set for the Gd atom and TZVP for all the other atoms.

For MOLCAS calculations, basis sets for all atoms were taken from the ANO-RCC library as implemented in the MOLCAS package. All the calculations were carried out using complete active space (CAS). In the case of Dy, the active space is comprised of nine active electrons of Dy (III) in the seven 4f active orbitals (RAS (9,7)), while in Er (III), the number of 4f electrons is 11 (RAS (11, 7)). The CASSCF calculations were performed with the same basis sets and active spaces to obtain relative energies of the Kramers doublets (KDs). For Dy (III), 21 roots in the sextet state, while for Er (III), 35 roots in quartets have been used in the configuration interaction (CI) procedure. Once these spin-free excited states are obtained, we mixed all of these states by using the RASSI-SO module to compute the spin-orbit coupled states.

Acknowledgements

PD thanks PMRF for the fellowship. AS thanks CSIR for the fellowship. GR would like to thank DST and SERB (SB/SJF/2019-20/12; CRG/2022/001697) for funding.

Conflict of Interests

The authors declare no conflict of interest.

Data Availability Statement

The data that support the findings of this study are available in the supplementary material of this article.

Keywords: Carbon dioxide · Density Functional Theory · CASSCF · Spin-Orbit coupling · 3d–4f catalysts

[1] M. Aresta, A. Dibenedetto, *Dalton Trans.* **2007**, 2975–2992.
[2] N. Dimitratos, J. A. Lopez-Sanchez, G. J. Hutchings, *Top. Catal.* **2009**, *52*, 258–268.
[3] L. Zhang, Z. Han, X. Zhao, Z. Wang, K. Ding, *Angew. Chem. Int. Ed.* **2015**, *54*, 6186–6189.
[4] P. Daw, *J. Am. Chem. Soc.* **2017**, *139*, 11722–11725.
[5] Y. Zhang, A. D. MacIntosh, J. L. Wong, E. A. Bielinski, P. G. Williard, B. Q. Mercado, N. Hazari, W. H. Bernskoetter, *Chem. Sci.* **2015**, *6*, 4291–4299.
[6] A. Sen, G. Rajaraman, *Inorg. Chem.* **2023**, *62*, 2342–2358.
[7] A. Álvarez, M. Borges, J. J. Corral-Pérez, J. G. Olcina, L. Hu, D. Cornu, R. Huang, D. Stoian, A. Urakawa, *ChemPhysChem* **2017**, *18*, 3135–3141.
[8] C. Ziebart, C. Federsel, P. Anbarasan, R. Jackstell, W. Baumann, A. Spannenberg, M. Beller, *J. Am. Chem. Soc.* **2012**, *134*, 20701–20704.
[9] A. C. Kathalikkattil, R. Babu, R. K. Roshan, H. Lee, H. Kim, J. Tharun, E. Suresh, D.-W. Park, *J. Mater. Chem. A* **2015**, *3*, 22636–22647.
[10] Z. Zhou, C. He, J. Xiu, L. Yang, C. Duan, *J. Am. Chem. Soc.* **2015**, *137*, 15066–15069.
[11] P. Comba, L. R. Gahan, G. R. Hanson, M. Maeder, M. Westphal, *Dalton Trans.* **2014**, *43*, 3144–3152.
[12] S. Sabater, M. Menche, T. Ghosh, S. Krieg, K. S. Rück, R. Paciello, A. Schäfer, P. Comba, A. S. K. Hashmi, T. Schaub, *Organometallics* **2020**, *39*, 870–880.
[13] A. Sen, M. Ansari, G. Rajaraman, *Inorg. Chem.* **2023**, *62*, 3727–3737.
[14] H. Yang, G. Gao, W. Chen, L. Wang, W. Liu, *Dalton Trans.* **2020**, *49*, 10270–10277.
[15] N. Qiao, X.-Y. Xin, X.-F. Guan, C.-X. Zhang, W.-M. Wang, *Inorg. Chem.* **2022**, *61*, 15098–15107.
[16] Z. Han, Y. Zhao, G. Gao, W. Zhang, Y. Qu, H. Zhu, P. Zhu, G. Wang, *Small* **2021**, *17*, 2102089.
[17] F. Castro-Gómez, G. Salassa, A. W. Kleij, C. Bo, *Chem. Eur. J.* **2013**, *19*, 6289–6298.
[18] G. Bresciani, M. Bortoluzzi, F. Marchetti, G. Pampaloni, *ChemSusChem* **2018**, *11*, 2737–2743.
[19] A. Ramesh, S. De, S. Bajaj, B. Das, S. Ray, *Eur. J. Inorg. Chem.* **2024**, *27*, e202300610.
[20] C.-H. Guo, J.-Y. Song, J.-F. Jia, X.-M. Zhang, H.-S. Wu, *Organometallics* **2010**, *29*, 2069–2079.
[21] S. Kozuch, S. Shaik, *Acc. Chem. Res.* **2011**, *44*, 101–110.
[22] N. Barooah, M. Sundararajan, J. Mohanty, A. C. Bhasikuttan, *J. Phys. Chem. B* **2014**, *118*, 7136–7146.
[23] G. Rajaraman, F. Totti, A. Bencini, A. Caneschi, R. Sessoli, D. Gatteschi, *Dalton Trans.* **2009**, *17*, 3153–3161.
[24] M. M. Hanninen, A. J. Mota, R. Sillanpaa, S. Dey, G. Velmurugan, G. Rajaraman, E. Colacio, *Inorg. Chem.* **2018**, *57*, 3683–3698.
[25] Y.-M. Shen, W.-L. Duan, M. Shi, *J. Org. Chem.* **2003**, *68*, 1559–1562.
[26] A. Sen, A. Ansari, A. Swain, B. Pandey, G. Rajaraman, *Inorg. Chem.* **2023**, *62*, 14931–14941.
[27] S. Dey, T. Sharma, A. Sarkar, G. Rajaraman, in *Computational Modelling of Molecular Nanomagnets*, Springer, **2023**, pp. 291–394.
[28] M. Frisch, G. Trucks, H. Schlegel, G. Scuseria, M. Robb, J. Cheeseman, G. Scalmani, V. Barone, B. Mennucci, G. Petersson, *See also: URL:* http://www.gaussian. com **2009**.
[29] F. Aquilante, J. Autschbach, R. K. Carlson, L. F. Chibotaru, M. G. Delcey, L. De Vico, I. F. Galván, N. Ferré, L. M. Frutos, L. Gagliardi, Wiley Online Library, **2016**.
[30] a) J. Tirado-Rives, W. L. Jorgensen, *J. Chem. Theory Comput.* **2008**, *4*, 297–306; b) C. Lee, W. Yang, R. G. Parr, *Phys. Rev. B* **1988**, *37*, 785.
[31] T. R. Cundari, S. O. Sommerer, L. A. Strohecker, L. Tippett, *J. Chem. Phys.* **1995**, *103*, 7058–7063.
[32] T. R. Cundari, W. J. Stevens, *J. Chem. Phys.* **1993**, *98*, 5555–5565.
[33] R. Ditchfield, W. J. Hehre, J. A. Pople, *J. Chem. Phys.* **1971**, *54*, 724–728.
[34] R. B. Ross, S. Gayen, W. C. Ermler, *J. Chem. Phys.* **1994**, *100*, 8145–8155.
[35] J. J. Jesudas, C. T. Pham, A. Hagenbach, U. Abram, H. H. Nguyen, *Inorg. Chem.* **2019**, *59*, 386–395.
[36] P. Richardson, T.-J. Hsu, C.-J. Kuo, R. J. Holmberg, B. Gabidullin, M. Rouzières, R. Clérac, M. Murugesu, P.-H. Lin, *Dalton Trans.* **2018**, *47*, 12847–12851.
[37] E. Colacio, J. Ruiz, A. J. Mota, M. A. Palacios, E. Cremades, E. Ruiz, F. J. White, E. K. Brechin, *Inorg. Chem.* **2012**, *51*, 5857–5868.
[38] S. I. Gorelsky, A. Lever, *J. Organomet. Chem.* **2001**, *635*, 187–196.

Manuscript received: May 7, 2024
Accepted manuscript online: May 21, 2024
Version of record online: June 28, 2024